Fluid Dynamics &
Materials Processing

Tech Science Press

http://doi.org/10.32604/fdmp.2026.078680

ARTICLE

Effect of Surface Hydrophilicity and Hydrophobicity on Droplet Behavior in Tiny Rectangular Flow Channels

Jian Li[1,2,*], Kexiang Wen[1], Jian Wei[1], Dengke Wen[1] and Ruihao Sun[1]

[1]Henan International Joint Laboratory of Energy Conservation and Pollutant Control Technology for Energy Power Devices, Henan University of Science and Technology, Luoyang, China
[2]College of Mechanical Engineering, Tianjin University, Tianjin, China
*Corresponding Author: Jian Li. Email: jianlee127@haust.edu.cn

Received: 06 January 2026; Accepted: 14 April 2026; Published: 07 May 2026

ABSTRACT: The effective management of gas–liquid two-phase flow, emerging within the microchannels of proton exchange membrane fuel cells (PEMFCs) during operations, is crucial for improving energy conversion efficiency. In this study, the influence of surface wettability is examined for hydrophilic and hydrophobic conditions through a visualization-based experimental setup focused on single-droplet dynamics. The impact of key parameters on droplet behavior is systematically explored, while the mechanisms underlying the observed flow patterns are elucidated and the coupling among governing physical factors is clarified. The results show that, under comparable conditions, hydrophobic surfaces exhibit larger advancing contact angles and greater contact-angle hysteresis. At low Reynolds numbers, they also display higher receding contact angles. In addition, droplets on hydrophobic surfaces present consistently smaller infiltration diameters than those on hydrophilic ones, indicating a stronger tendency to detach under imposed flow conditions.

KEYWORDS: Visual experiment; tiny channel; gas-liquid flow; single droplet; surface characteristics

1 Introduction

In proton exchange membrane fuel cells (PEMFC), fine liquid droplets form on the surface of the gas diffusion layer and gradually increase in size as the electrochemical reaction proceeds. These droplets increase airflow resistance. If not removed in a timely manner, excessive water accumulation can block the gas diffusion channel [1], ultimately resulting in flooding [2]. Therefore, a thorough understanding of liquid water transport within fuel-cell layers is essential for the stable operation of PEMFC [3]. Nilanjan Mondal et al. [4] quantitatively predicted the enhancement in water-removal efficiency induced by microstructures. They found that the hydrophobic microstructures reduced the dominance of viscous force over inertia and capillary force. This promoted end-pinching or truncation at the droplet neck, thereby reducing the production of undesired satellite droplets that could lead to chamber flooding. Their work showed that an appropriate combination of substrate structure and jet-velocity-induced shear can suppress satellite droplet generation and shorten breakup time, thereby significantly enhancing PEMFC water-removal efficiency. Studies by Zhu et al. [5] and Cai et al. [6] investigated how gas diffusion layer (GDL) wettability influences liquid water behavior in the channel. The results indicated that a hydrophobic GDL surface facilitates droplet detachment from the porous structure and thus accelerates droplet removal. Golamreza Molaeimanesh and colleagues [7] employed the Lattice-Boltzmann Method (LBM) to simulate the dynamic behavior of water droplets during removal from the gas diffusion layer (GDL) of PEMFC electrodes under an interdigitated flow field. Their study also examined the effects of GDL wettability and its spanwise and transverse variations on removal performance. The findings underscored the important role of wettability and its directional gradients in governing droplets dynamic during the removal process. Chen et al. [8] used the VOF method to investigate the effect of surface microstructure on transport and reported that a GDL surface with carbon paper fibers aligned parallel to the airflow direction facilitates droplet removal. To better understand droplet behavior, the droplet can be studied separately from the fuel cell system as an independent flow phenomenon.

Therefore, investigating droplet dynamics on solid surfaces is of great significance. Nilanjan Mondal et al. [9] studied the combined effects of surface patterning and droplet properties on the oscillation behavior of the droplet after impact. They further incorporated different levels of roughness by mimicking patterned surfaces. The results that showed surface topography significantly affected the wetting state, impact dynamics, and oscillation behavior of droplets. In addition, surface patterning was found to regulate the wetting state, allowing transitions from Wenzel state to Cassie state.

Flow-field design is crucial for mitigating droplet accumulation in PEMFCs. Fatemeh Bagherighajari et al. [10] investigated fuel-cell flow fields and demonstrated that a high rib-to-channel width ratio led to reduced cell performance due to liquid-water accumulation in the rib region. In addition, at a low relative humidity of RH = 25%, interdigitated type II achieved 10.4% higher performance than that at RH = 100%, owing to more effective over-rib convection and enhanced water removal. Abbas Moradi Bilondi et al. [11] proposed replacing portions of the solid ribs segments in the flow-field design with porous carbon inserts (PCI). These inserts enhanced the removal of liquid water accumulate on the rib surfaces along the cathode flow channel, thereby reducing the risk of flooding. A. Hamrang et al. [12] compared the water-removal capacity of conventional parallel serpentine flow fields (PSFF) and parallel serpentine baffle flow fields (PSBFF), and found that PSBFF was more effective in removing water from porous regions under all conditions examined.

Channel-wall wettability strongly affects gas-liquid two-phase flow in microchannels [13]. Surface modifications can transform a hydrophilic surface into a hydrophobic one [14]. At present, superhydrophobic surfaces are mainly prepared by two approaches: applying hydrophobic coatings and constructing surface microstructure [15]. Fluorinated polymers are regarded as promising materials because of their flexibility and excellent mechanical, chemical and thermal stability [16–18]. Nanocomposite based on polyvinylidene fluoride (PVDF) and TiO_2-SiO_2 can impart hydrophobicity to solid surface [19]. When copper (Cu) and stainless-steel (SS304) surfaces are treated by femtosecond laser irradiation, the stainless-steel surface becomes hydrophobic immediately, whereas the copper surface evolves into a stable superhydrophobic state after almost 90 days [20]. The combination of a femtosecond laser with Ti_3C_2 MXene and hydrophobic SiO_2 nanoparticles enables the fabrication of a robust electrothermal superhydrophobic surface with a contact angle of up to 160.3° [21]. On a titanium alloy substrate, a surface prepared using a technique that couples laser microstructuring with hydrothermal deposition exhibits a contact angle of 160.5° and a rolling angle of only 1°, and significantly influences droplet impact behavior [22]. J. P. Owejan et al. [23] and Chun et al. [24] used PTFE to hydrophobically treat the flow channel, and their results showed that PTFE coating reduced droplet accumulation and promoted droplet detachment. A study by Wang et al. [25] showed that a titanium felt gas diffusion layer coated with 3 wt% PTFE could achieve a power density of up to 183 mW/cm^2 under humid conditions and exhibited the lowest current fluctuations in stability tests. Furthermore, solvent optimization can further improve interfacial compatibility on the PTFE surface, significantly enhancing the membrane's durability [26]. Fatma Gül Boyaci San et al. [27] investigated how fluoropolymer-based additives, with different additive-to-binder and additive-to-filler ratios, affected the wettability of polymer-composite bipolar plates. Their results indicated that increasing the fluoropolymer content relative to filler and binder significantly enhanced surface hydrophobicity. Furthermore, the dynamic behavior of droplets within microchannels is also critical for micro-mixer design and emulsion control. For example, Yu et al. [28] investigated the effects of different geometric structures and wall wettability on droplet formation and internal circulation through numerical simulations, noting that wall properties are key factors determining the contact state between droplets and the channel walls.

Contact-angle hysteresis is a key parameter in two-phase flow on a wet surface [29], and low contact-angle hysteresis is an important characteristic of superhydrophobic surfaces [30]. This phenomenon arises from multiple factors, including surface roughness, heterogeneity in surface microchemical properties, droplet-size effects, the orientation and deformation of surface molecules, and liquid infiltration into cracks on the solid surface [31]. As surface roughness and liquid surface tension increase, contact-angle hysteresis also increases [32]. Chen et al. [33] developed simplified models based on macroscopic force equilibrium and approximate droplet geometries, and compared the predicted instability patterns, or "windows," with experimental observations. Their study showed that droplet detachment efficiency could be enhanced by increasing flow-channel length and mean gas velocity, reducing channel height and contact-angle hysteresis, and improving the hydrophobicity of the GDL/GFC interface.

Wettability is a key property of hydrophobic surfaces and is generally characterized by the equilibrium contact angle θ [34]. A surface is generally considered hydrophilic when the contact angle $\theta < 90^\circ$; otherwise, it is regarded as hydrophobic. Hypsometry and goniometry are the most commonly used methods for contact-angle measurement [35], and both are primarily designed for gas-liquid-solid system. With slight modifications, these methods, can also be applied to determine the contact angle in liquid-liquid-solid system [36–39].

This study analyzed the forces acting on a single droplet in a microchannel and established the mechanical relationship governing droplet behavior under airflow. Because the contact angle is directly related to the surface energies of gas, liquid and solid phases at the three-phase contact line, it depends on the material properties and surface roughness of the plate. However, quantitatively determining the influence of these solid-surface properties on the contact angle remains difficult. Since the experimental substrate was a smooth stainless-steel plate, the effect of surface roughness on the contact angle was neglected. This study employed a self-assembled molecular film method for hydrophobic surface treatment. The results indicate that the self-assembled molecular film has a smooth and even surface, can improve the surface condition of the substrate, possesses low surface energy, and exhibits hydrophobic properties and good lubricating performance [40]. To reduce measurement error, the five-point fitting method was employed to measure the advancing and receding contact angle of the droplet. Each angle was measured five times, and the average value was then taken. Based on experiments conducted under two different surface wettabilities, hydrophilic and hydrophobic, with the other flow parameters kept constant, the relationships among Reynolds number, contact angle, droplet height, and infiltration diameter were obtained.

2 Theoretical Analysis

2.1 Young Equation

In 1805, Young proposed the equation describing the equilibrium of interfacial forces, as follows:

$$\cos\theta = \frac{\sigma_{SG}-\sigma_{SL}}{\sigma_{LG}} \tag{1}$$

In this equation, σ_{SG}, σ_{SL} and σ_{LG} denote the interfacial tensions at the solid-gas, solid-liquid and gas-liquid interfaces, respectively. Young suggested that the contact angle formed at the junction of three phases is determined by the balance of surface tensions. Alternatively, the contact angle can also be derived based on the principle of minimizing the overall free energy of the system [41]. According to Young's equation [42], when a droplet is at equilibrium, the contact angle can be uniquely determined.

In practical analysis, contact angle hysteresis induced by the surface characteristics of real walls should be taken into account. In this case, the contact angle is not uniquely defined, but varies continuously within a certain range, exhibiting a multivalued nature. The maximum value of the contact angle is called the advancing angle, whereas the minimum value is called the receding angle [30,43,44]. For real surface, Wang and Peng [45,46] proposed a hysteresis tension model to account for contact angle hysteresis. According to this model, a hysteretic tension exists at the contact line of a stationary droplet. Based on the Young's equation, the corresponding mechanical relationship is expressed as follows:

$$\cos\theta = \frac{\sigma_{SG}-\sigma_{SL}}{\sigma_{LG}} - \frac{f}{\sigma_{LG}} = \cos\theta_Y - \frac{f}{\sigma_{LG}} \tag{2}$$

In the equation, θ denotes the contact angle and satisfies $\theta_R < \theta < \theta_A$. Based on the above analysis, the advancing contact angle and the receding contact angle should satisfy the following relations, respectively:

$$\cos\theta_A = \cos\theta_Y - \frac{f_{\max}}{\sigma_{LG}} \tag{3}$$

$$\cos\theta_R = \cos\theta_Y - \frac{f_{\min}}{\sigma_{LG}} \tag{4}$$

The droplet is subjected to a wind force F_D, and at the critical wind speed, f reaches its extreme value at both the front and rear of the droplet contact line under the action of the external airflow. Surface tension and hysteretic tension act on the three-phase contact line. Owing to droplet deformation, the contact angle along the three-phase contact line continuously varies from the receding angle θ_R to the advancing angle θ_A, as shown in Fig. 1. The droplet interface shape at the critical wind speed is first determined, which depends on the droplet volume, infiltration diameter, advancing contact angle, and receding contact angle. Therefore, the variation pattern of the contact angle around the droplet contact line can be obtained. Under the determined critical shape, the surface tension of the droplet remains constant, whereas the wind force depends on the incoming flow velocity and increases with increasing incoming flow velocity. When the wind force equals the surface force, the droplet detaches from the wall. The critical wind speed for droplet detachment can then be deduced from this mechanical equilibrium relationship.

2.2 Droplet Force Analysis

The coordinate system is established as shown in Fig. 1. The solid-liquid interface is circular, and the droplet detachment diameter is d_c. β is the included angle shown in Fig. 1, and θ denotes the solid–liquid contact angle corresponding to β. The airflow passes over the horizontal plate along the OX axis, and the droplet deforms under the action of the wind. With a gradual increase in wind velocity, the contact angle on the windward side decreases, whereas that on the leeward side increases. At the critical wind speed, the contact angle on the windward side corresponds to the receding angle, while that on the leeward side corresponds to the advancing angle. Due to droplet deformation, the contact angle along the three-phase contact line continuously varies from the receding angle θ_R to advancing angle θ_A. If point A (X, 0, Z) is taken on the three-phase contact line, it is acted on by σ_{SG}, σ_{SL}, σ_{LG} and hysteresis tension f. Therefore, f must satisfy the following condition:

$$f = \sigma_{LG}\cos\theta + \sigma_{SL} - \sigma_{SG} \tag{5}$$

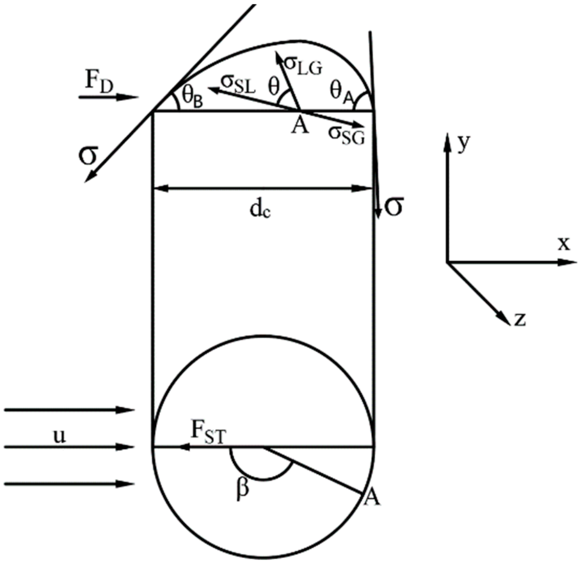

Figure 1: Force analysis of a droplet under incoming flow.

Since σ_{LG} is an internal force, the integral of σ_{SL} and σ_{SG} along the entire circumference are zero. Therefore, the resultant force of the above four forces can be expressed as follows:

$$F_{ST_x} = \left|\oint \overline{f} dl\right| = \oint f\cos\beta dl = \oint (\sigma_{LG}\cos\theta + \sigma_{SL} - \sigma_{SG})\cos\beta dl =$$

$$\oint \sigma_{LG}\cos\theta\cos\beta dl = 2\int_0^x \sigma_l\cos\theta\cos\beta(d_c/2)d\beta \tag{6}$$

If the solid-liquid contact angle is assumed to vary linearly along the bottom perimeter of the droplet [47], then:

$$\theta = [(\theta_A - \theta_R)/\pi]\beta + \theta_R \tag{7}$$

$\theta = \theta_R$ when $\beta = 0$ and $\theta = \theta_A$ when $\beta = \pi$.

By substituting Eq. (7) into Eq. (6) and performing the integration, the following expression is obtained:

$$F_{ST_x} = \sigma_l d_c(\pi/2)(\sin\theta_A + \sin\theta_R)\left\{\frac{1}{[\pi - (\theta_A - \theta_R)]} - \frac{1}{[\pi + (\theta_A - \theta_R)]}\right\} \tag{8}$$

The wind force acting on the droplet is given by the following hydrodynamic relation:

$$F_D = \frac{1}{2}C_D A\rho\overline{u}_{droplet}^2 \tag{9}$$

C_D is the drag coefficient of the droplet, A is the windward area of the droplet, and $\overline{u}_{droplet}$ is the average gas flow velocity over the droplet surface. Experiments on the detachment of the wall-adhering bubbles under external incoming flow have been carried out for a pipe diameter of 19 mm. Previous studies have shown that when $20 < \mathrm{Re} < 400$, C_D can be taken as 1.2 [48] and this value is also applicable to droplet detachment in an open environment [45]. However, in confined spaces and under high Reynolds number conditions, local flow velocities increase significantly, leading to an increase in the actual drag coefficient.

The velocity distribution in a rectangular flow channel can be approximated using a quadratic function. A coordinate system is established at an arbitrary point in the channel, as shown in Fig. 2. According to the continuity equation for an incompressible fluid, the velocity component in the x-direction is zero. Shear stress is neglected and the flow is assumed to be steady.

$$u(y,z) = \left(A_1 + B_1 y + C_1 y^2\right)\left(A_2 + B_2 z + C_2 z^2\right) \tag{10}$$

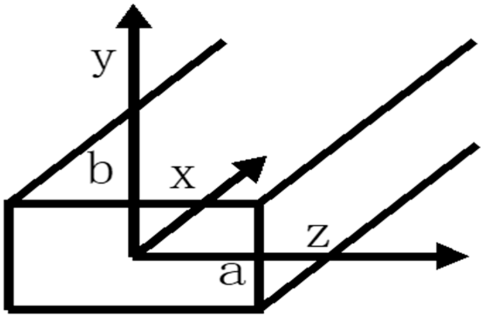

Figure 2: Channel structure.

The fluid momentum equation in the flow channel is given by:

$$\frac{\partial u_i}{\partial t} + u_j \frac{\partial u_i}{\partial x_j} = F_i - \frac{1}{\rho}\frac{\partial p}{\partial x_i} + \nu \nabla^2 u_i \tag{11}$$

According to the continuity equation for an incompressible fluids, $\frac{\partial u}{\partial t} = 0$, so for parallel flows, $v = 0$, $w = 0$.

Neglecting shear stress, the flow is assumed to be in a steady state, and the momentum equation can be simplified as follows:

$$\left(\frac{\partial^2 u}{\partial y^2} + \frac{\partial^2 u}{\partial z^2}\right) = \frac{1}{\mu}\frac{dp}{dx} \tag{12}$$

The resulting velocity distribution is as follows:

$$u(y,z) = \frac{9}{4}\frac{\overline{u}}{a^2 b^2}\left(b^2 - y^2\right)\left(a^2 - z^2\right) \tag{13}$$

$\overline{u}$ is the average velocity of the incoming flow:

$$\overline{u}_l = \frac{\iint\limits_{D_{xy}} u(x,y)\,dx\,dy}{A} \tag{14}$$

$\overline{u}_l$ is the average velocity of the droplet on the windward side; and A is the windward area of the droplet.

When the droplet is in force equilibrium:

$$F_{ST} = F_D \tag{15}$$

3 Experimental System

All experiments were conducted at room temperature. A schematic diagram of the experimental system can be shown in Fig. 3. The experimental procedure was as follows: the gas first passed through a dust filter before entering the transparent rectangular flow microchannel. After filtration, the gas was delivered into the flow stabilisation tank by a WM-2H oil-free air compressor, and then entered the transparent flow channel after the flow rate was adjusted by a PM1000A flow controller to ensure a uniform and steady airflow. A stainless-steel horizontal plate located at the bottom of the flow channel was equipped with micropores of 100 and 200 μm in diameter, and pure water was injected into the microchannel through these by a peristaltic pump. As the injected liquid volume increased continuously, the droplets gradually grew. The OLYMPUS i-SPEED 3 high-speed camera system was used to record morphological changes of droplets during their formation and detachment in the microchannel. The high-speed camera has a frame rate of 2000 frames per second, with a maximum of 150,000 frames per second; the exposure time is 1 μs. The recorded image data were then processed and analyzed to determine the droplet height and contact angle at different times. To ensure airflow stability and facilitate macroscopic observation of droplet motion, the flow channel length was set to 206 mm to ensure that the airflow has fully developed into a uniform and stable flow by the time the sample enters the observation zone, thereby eliminating any impact of airflow turbulence on contact angle measurements. To better visualize droplet shape evolution and detachment in the rectangular microchannel, a stainless-steel plate was used at the bottom of the experimental section, while optical glass plates were used on the other three sides. Ultraviolet glue with minimal influence on visualisation was used to bond these four parts together, thereby forming a rectangular microchannel for visualisation. This setup was used to observe droplet deformation in the microchannel.

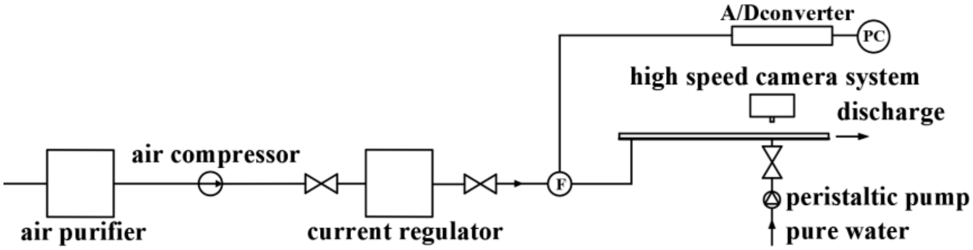

Figure 3: Experimental system diagram.

Twelve experimental plates were selected, corresponding to three different flow-channel cross-sectional areas (1.2 × 1.2 mm/2.2 × 2.2 mm/3.2 × 3.2 mm), and a total of 24 flow channels were constructed. Due to the large aspect ratio of the microchannel, the flow was simplified as two-dimensional. Since the experimental baseplate was made of smooth stainless steel, the effect of surface roughness on the contact angle was neglected in this study.

The advancing and receding contact angle of the droplet in the rectangular microchannel changed dynamically under the action of incoming airflow. The contact-angle difference is a physically important quantity governing the equilibrium and detachment of droplets under airflow. In this experiment, changes in droplet contact angle were measured under different Reynolds numbers, micropore sizes, droplet heights, and channel sizes. In this experiment, the droplet contact angle was measured using a CA500 contact angle measurement device. The resulting droplet adhered to the substrate surface and cast a shadow. The projection-screen micrometer uses optical magnification to project the image onto a screen. The droplet contact angle was determined using the five-point fitting method, in which two points were selected at the droplet–solid interface to establish a reference line. Then, three points were selected at the bottom, middle and top of one side of the droplet, depending on whether the advancing or receding angle was to be measured. Because these points were selected manually, they were chosen as close as possible to the droplet profile, and the software automatically marks them. These points are indicated by the red cross on the right side of the droplet in Fig. 4. Finally, the software automatically fitted the profile and calculated the contact angle, so each measurement directly yielded the fitted advancing and receding angles. The blue and green dots in the figure indicate the upper and lower positions calculated by the software. We performed five independent replicate measurements of the contact angle for each characteristic state. The results of the five measurements showed a high degree of consistency, and the properties of the surfaces used remained stable throughout the experiment.

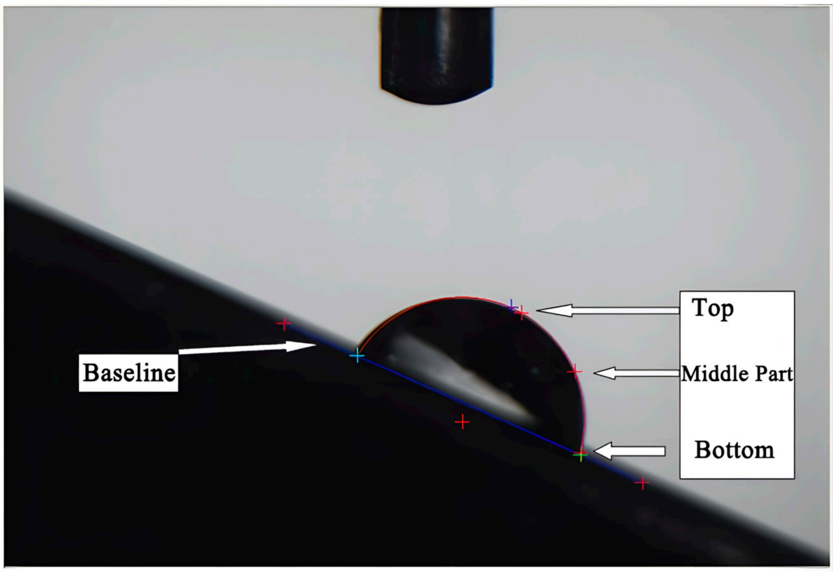

Figure 4: Measuring contact angle by five-point fitting method.

Fig. 5 shows the dynamic evolution of a droplet on a hydrophobic surface with a bottom-hole diameter of 100 μm, and a flow-channel cross sectional of 3.2 mm × 3.2 mm and Re = 3000. The images present the droplet morphology at different times, from the onset of droplet formation at the injection hole to the completion of droplet detachment from the hole. Fig. 6 illustrates the droplet formation process on hydrophobic and hydrophilic surfaces when the airflow is zero. The diameter of the bottom holes in both surfaces is 100 μm, and the cross sectional of the flow channels is 3.2 mm × 3.2 mm.

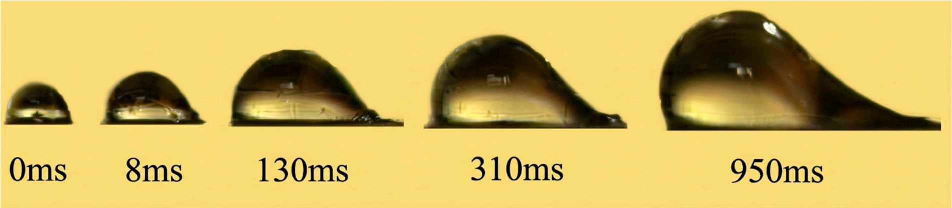

Figure 5: The existence states of droplets in the flow channel at different times.

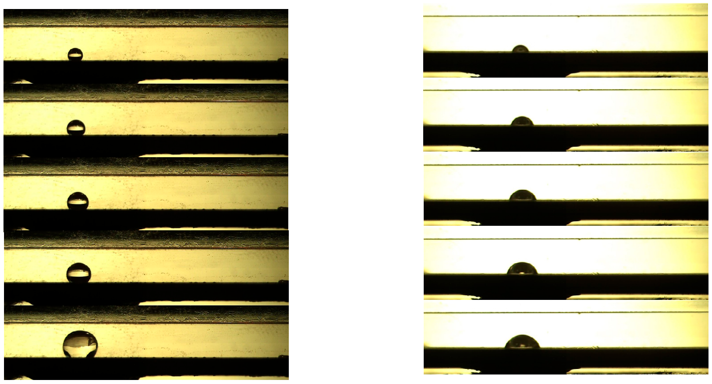

Figure 6: The process of droplet formation on hydrophobic and hydrophilic surfaces.

4 Experimental Results and Discussions

The effects of the flow-channel, air velocity and droplet size on droplet morphology were investigated experimentally. The phenomena on the hydrophilic and hydrophobic surfaces under different conditions were then analyzed and compared. The main comparative results are summarized as follows.

Figs. 7–9 show the relationship between the advancing contact angle θ_A and droplet height under different Reynolds numbers for two types of stainless-steel surface wettability, with a bottom-hole diameter of 100 μm and different channel widths and heights. It can be seen that the advancing contact angles θ_A on both surfaces increased with increasing droplet height, and that the effect of droplet height on θ_A became more pronounced as the Reynolds number increased. When the channel width was fixed, the influence of the channel height on θ_A was not obvious. This phenomenon can be explained as follows: at lower Reynolds numbers, the droplet was able to reach a greater height, whereas at higher Reynolds numbers, the droplet height decreased. When the flow-channel geometry is fixed, a larger droplet height indicates that the droplet experiences a stronger aerodynamic force and is therefore more likely to detach. Consequently, the droplet exhibits a stronger tendency to deform in the direction of the incoming airflow, as reflected by the increase in the advancing contact angle θ_A. However, it is difficult to quantify this relationship because θ_A is located on the leeward side of droplet, where the influencing factors are relatively complex. These factors include droplet surface tension, the flow-field redistribution caused by airflow bypassing the droplet, the increase in droplet infiltration diameter, and confinement effects from the side and top walls of the flow channel. In addition, experiments on hydrophobic surfaces showed that droplet detachment did not occur at all Re. Under low Reynolds number conditions (whether hydrophobic or hydrophilic), droplets tend to grow in place and eventually adhere to the side or top walls of the channel due to their large wetting area and strong adhesion, making it impossible for them to slide effectively along the flow direction. At low Reynolds numbers, the most common state of a droplet is to grow in place and undergo slight deformation until it eventually sticks to the side or top wall of the channel. At this point, it can be assumed that the droplet will not slide along the direction of the incoming flow. Experimental studies indicate that for hydrophobic surfaces, the maximum advancing angle does not always occur at the maximum Re; it frequently occurs at Re = 2000 or 2400. This phenomenon can be explained as follows: when Re = 2000 or 2400, the droplet's equilibrium state has reached its limit. Therefore, when Re continues to increase to 3000, the droplet reaches its critical equilibrium state before θ_A has fully increased, and the droplet is blown away by the incoming flow prematurely. Consequently, the critical detachment velocity of the droplet on a hydrophobic surface occurs at Re = 2000 or 2400. For hydrophilic surfaces, as Re increases from 2000 to 3000, the advance angle continues to increase, and the droplet has not yet reached its equilibrium limit. It can be concluded that the critical detachment wind speed of the droplet on a hydrophobic surface is lower than that on a hydrophilic surface.

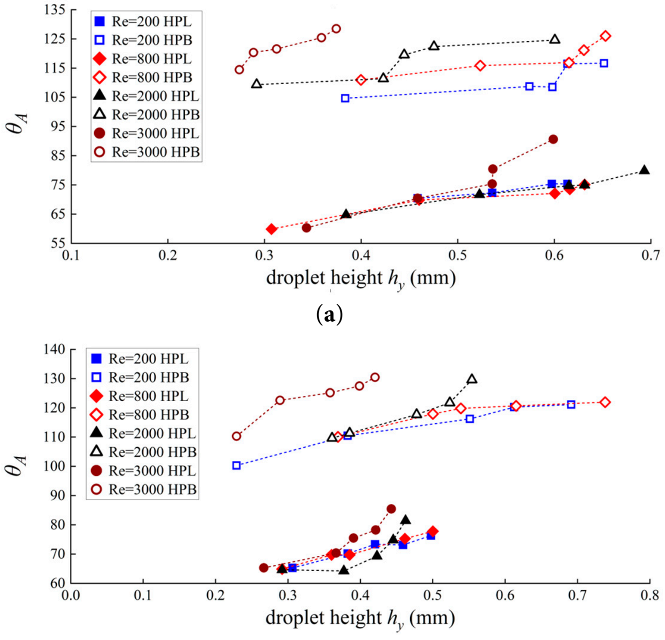

(**a**)

(**b**)

Figure 7: Relationship between advancing contact angle θ_A (°) and droplet height h_y (mm) under the action of incoming flow for a channel with a width of 1.2 mm: (**a**) Channel height 0.9 mm; (**b**) Channel height 2 mm.

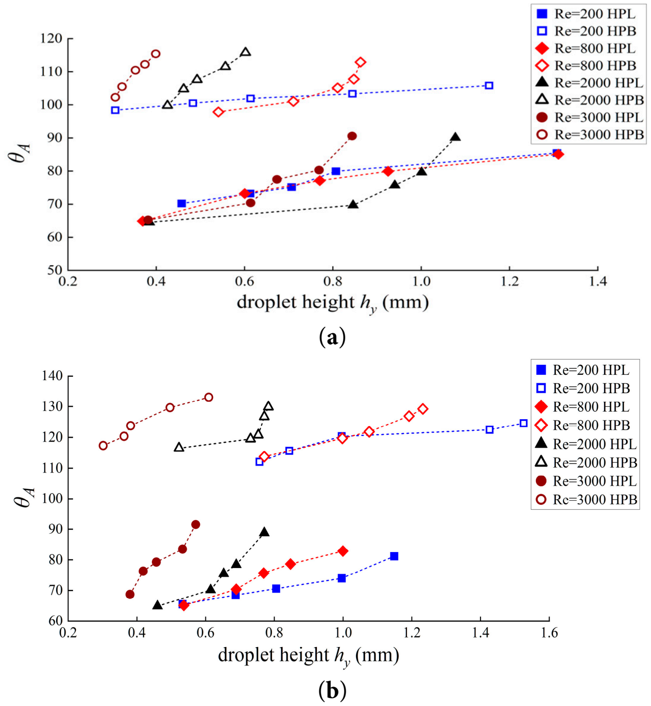

(**a**)

(**b**)

Figure 8: Relationship between advancing contact angle θ_A (°) and droplet height h_y (mm) under the action of incoming flow for a channel with a width of 2.2 mm: (**a**) Channel height 1.8 mm; (**b**) Channel height 2.9 mm.

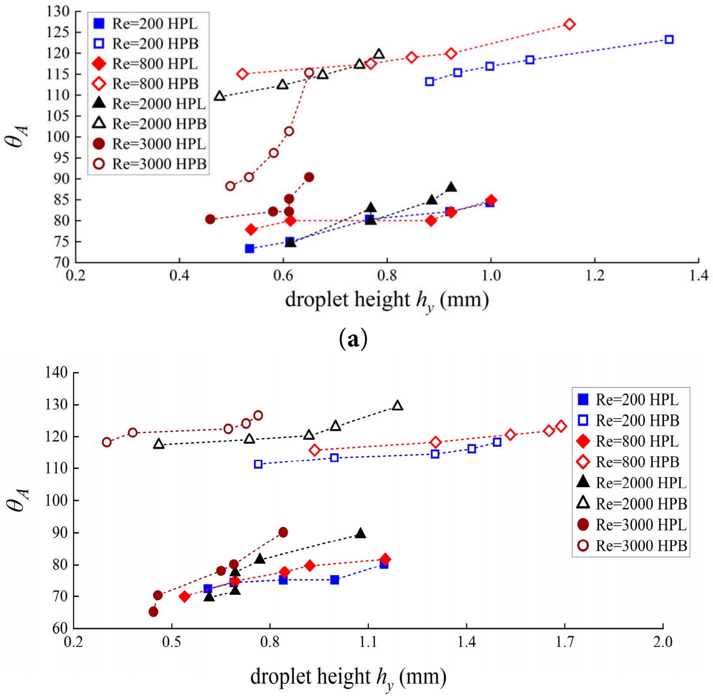

(**a**)

(**b**)

Figure 9: Relationship between advancing contact angle θ_A (°) and droplet height h_y (mm) under the action of incoming flow for a channel with a width of 3.2 mm: (**a**) Channel height 2 mm; (**b**) Channel height 3.2 mm.

Figs. 10–12 illustrate the relationship between the receding contact angle θ_R and droplet height under different Reynolds numbers for two types of stainless-steel surface wettability, with different channel width and height. Since the receding contact angle is located on the windward side of the droplet, the dominant factor affecting contact angle θ_R is the average airflow velocity over the droplet surface. At a constant Re and fixed flow-channel dimensions, θ_R on both surfaces generally decreased with increasing droplet height. Overall, the higher the Re, the more pronounced the effect of droplet-height variation on θ_R. For a fixed droplet height, a higher Re resulted in a smaller θ_R, and this trend was more evident on the hydrophobic surface. At low Re numbers, the gas flow rate and the aerodynamic force acting on the droplet were both relatively small. As shown in the figures, θ_R did not vary significantly with increasing droplet height. It can therefore be concluded that when the gas-flow velocity is low, liquid surface tension plays a dominant role in droplet behavior, whereas the influence of gas flow on the contact angle is not significant. When the Re is high and the droplet height is large, θ_R becomes smaller because the aerodynamic force acting on the droplet increases significantly and eventually overcomes the constraint imposed by surface tension on droplet position and shape. As a result, the droplet is stretched in the direction of the incoming flow, leading to a reduction in θ_R. In contrast, when the Re is low, the effect of droplet height on θ_R is not obvious, because the influence of airflow on the droplet remains weak relative to surface tension. Therefore, at low Reynolds numbers, the droplet tends to grow in a direction perpendicular to the airflow, while the receding contact angle, θ_R remains close to its original value. Although the variation trend of θ_R is similar on both surfaces, there are significant quantitative differences between them. At low Re, the θ_R value on the hydrophobic surface is obviously larger than that on the hydrophilic surface, whereas at high Re, the θ_R value on the hydrophobic surface is generally smaller than that on the hydrophilic surface. This phenomenon can be explained as follows: At low Re, the droplet is subjected to a relatively weak aerodynamic force, resulting in only slight deformation and a greater tendency to maintain its static contact angle. In the experiment, the static contact angle of the hydrophobic surface was 107.5°, while that of the hydrophilic surface was 64.2°; the static contact angle of the hydrophobic surface was significantly greater than that of the hydrophilic surface. When Re is small, the surface tension of the droplet plays a dominant role in the forces acting on the droplet, and the effect of wind force on the change in droplet shape is limited. The retraction angle on the hydrophobic surface is significantly greater than that on the hydrophilic surface, and there is no significant difference in the deformation rate of the droplet on the two surfaces. However, when Re is large (2000 < Re < 3000), due to the lower adhesion of the hydrophobic surface to the droplet, the retraction angle on the windward side of the droplet exhibits greater sensitivity, and the droplet deformation rate is higher than that on the hydrophilic surface. This implies that under the same wind speed increment, droplets on the hydrophobic surface can adjust their geometry more rapidly. At the same time, we found a synergistic effect between the hydrophobic surface properties and the droplet height. When Re is high, changes in droplet height on the hydrophobic surface have a more pronounced effect on the retraction angle compared to the hydrophilic surface. Precisely because of the high sensitivity of θ_R on the hydrophobic surface, an increase in wind force resulting from the same height increment can induce a greater degree of deformation on the hydrophobic surface.

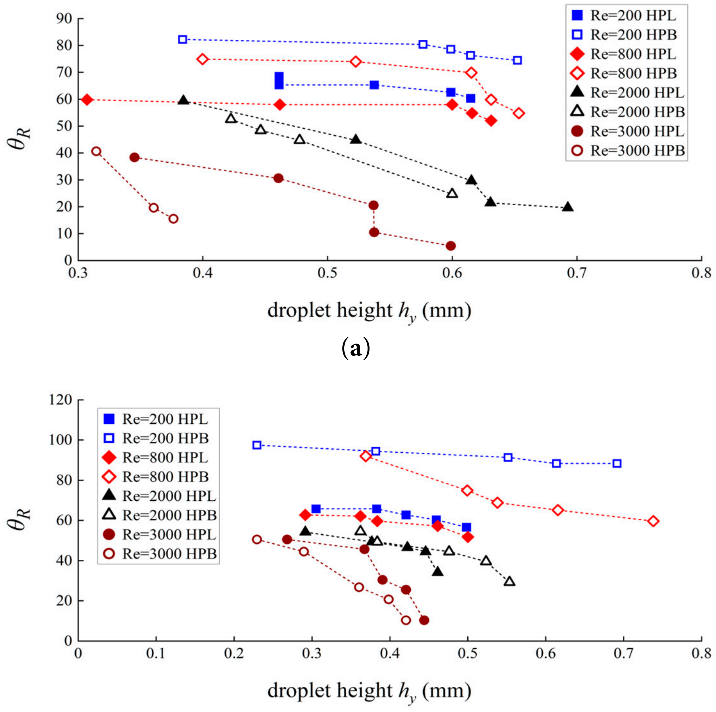

(**a**)

(**b**)

Figure 10: Relationship between receding contact angle θ_R (°) and droplet height h_y (mm) under the action of incoming flow for a channel with a width of 1.2 mm: (**a**) Channel height 0.9 mm; (**b**) Channel height 2 mm.

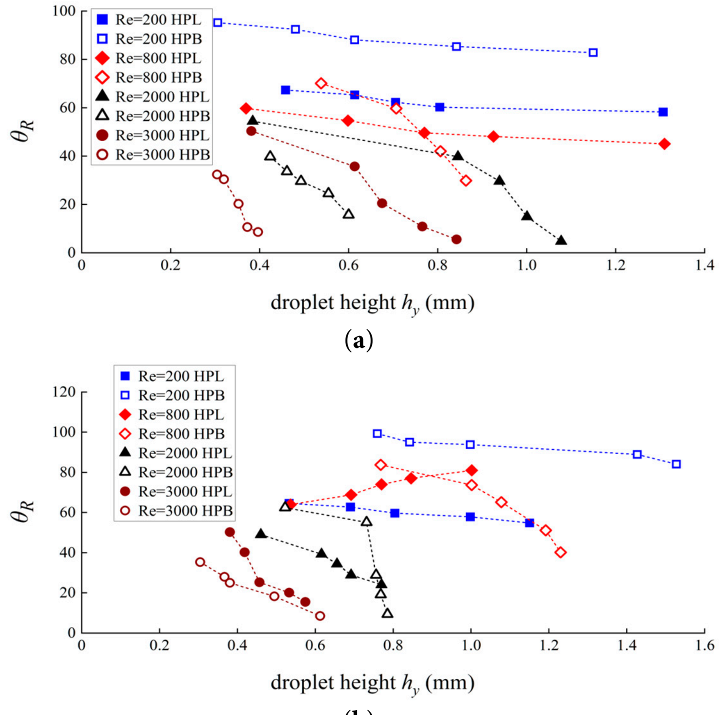

(**a**)

(**b**)

Figure 11: Relationship between receding contact angle θ_R (°) and droplet height h_y (mm) under the action of incoming flow for a channel with a width of 2.2 mm: (**a**) Channel height 1.8 mm; (**b**) Channel height 2.9 mm.

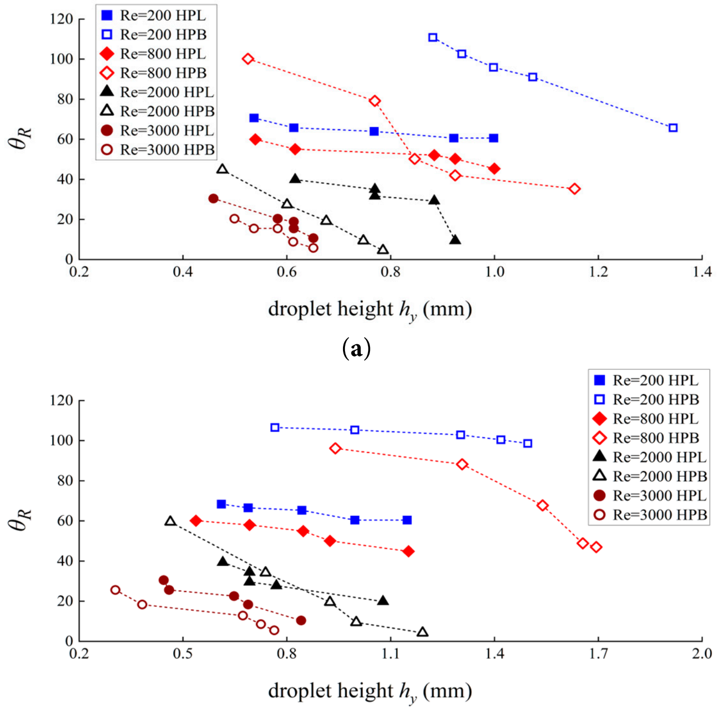

(**a**)

(**b**)

Figure 12: Relationship between receding contact angle θ_R (°) and droplet height h_y (mm) under the action of incoming flow for a channel with a width of 3.2 mm: (**a**) Channel height 2 mm; (**b**) Channel height 3.2 mm.

Figs. 13–15 show the relationship between the difference in contact angle $\Delta\theta$ and the droplet height under different Reynolds numbers for two types of stainless-steel surface wettability, with different channel width and height. As can be seen, when the droplet height was fixed, $\Delta\theta$ on both surfaces increased significantly with increasing Re. This indicates that the greater the deformation of the droplet on the stainless-steel surface, the higher the droplet instability and the droplet can detach from the surface. At the same time, when Re is constant, $\Delta\theta$ increases as droplet height increases, Meanwhile, when Re is small, the amplitude of $\Delta\theta$ increases less with increasing droplet height. This can be explained as follows: At low Reynolds numbers, droplet deformation under the incoming airflow was relatively small. In addition, the tendency of the droplet to detach was weak, making droplet separation more difficult and causing the droplet to accumulate and grow in place more easily. An increase in Re indicates that, under the same windward area, the force exerted by the incoming airflow on the droplet becomes larger. To maintain the force balance of the droplet on the stainless-steel surface, the hysteresis force increases, which is reflected by droplet spreading in the direction of the incoming airflow. We investigated the interaction between the Reynolds number and the channel height and found that there is a mechanism linking the channel height to the gas flow within the channel. Changes in the channel geometry affect the forces acting on the droplets by altering the local flow field distribution within the channel. Our results indicate that, when Re and the droplet height are held constant, $\Delta\theta$ decreases to some extent as the channel height increases. This is primarily because, as the channel height increases, the proportion of the droplet relative to the entire channel cross-section decreases. This implies that the degree of local acceleration caused by the droplet's disturbance of the airflow weakens, thereby reducing the drag effect of the surrounding airflow on the droplet. Consequently, the droplet undergoes less deformation, and $\Delta\theta$—which reflects the degree of droplet deformation—naturally becomes smaller. According to the figures, under the same Reynolds number, $\Delta\theta$ on the hydrophobic surface is generally larger than that on the hydrophilic surface, except when the Re is very low (Re = 200). Since $\Delta\theta$ is an important parameter for characterizing droplet stability, when the Re is high, it can be qualitatively inferred that the droplet is relatively easy to detach. However, this interpretation is not always applicable at low and medium Re, because $\Delta\theta$ is only meaningful for evaluating droplet detachment tendency when the droplet is close to the detachment state. At the same time, under low-Reynolds-number conditions, when the droplet is still far from detachment, a slightly larger $\Delta\theta$ on the hydrophilic surface than on the hydrophobic surface does not necessarily mean that the droplet can be separated more easily from the hydrophilic surface. As shown in the figure, at high Re, $\Delta\theta$ on the hydrophobic surface is clearly larger than that on the hydrophilic surface. Therefore, it can be qualitatively concluded that, under the action of incoming flow, droplet on the hydrophobic surface can detach more easily.

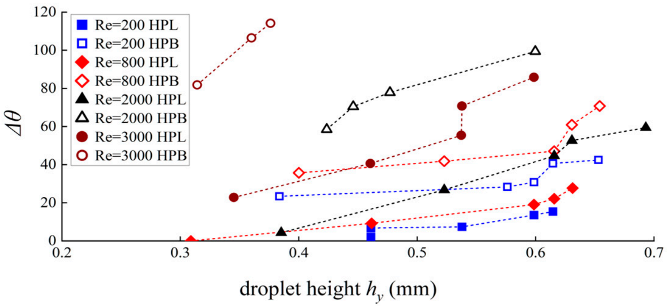

(**a**)

Figure 13: *Cont.*

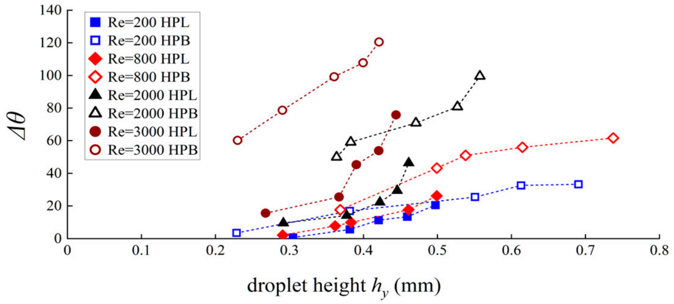

(**b**)

Figure 13: Relationship between the difference in contact angle $\Delta\theta$ (°) and droplet height h_y (mm) under the action of incoming flow for a channel with a width of 1.2 mm: (**a**) Channel height 0.9 mm; (**b**) Channel height 2 mm.

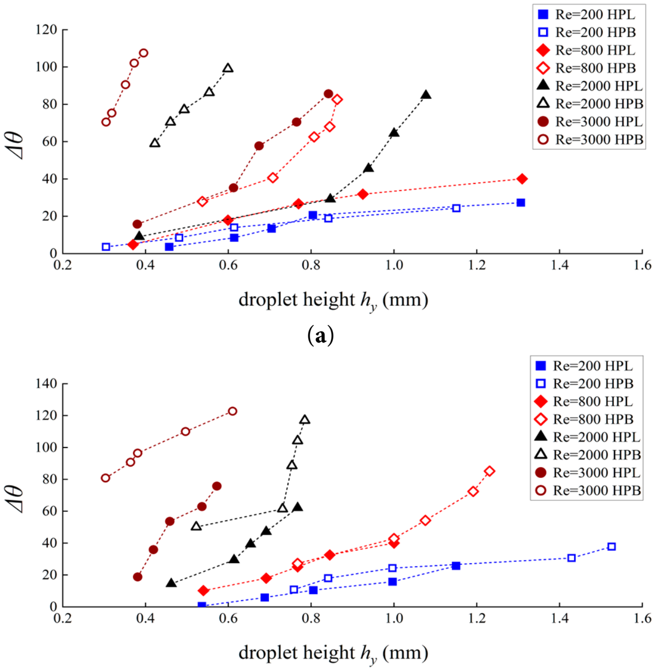

(**a**)

(**b**)

Figure 14: Relationship between the difference in contact angle $\Delta\theta$ (°) and droplet height h_y (mm) under the action of incoming flow for a channel with a width of 2.2 mm: (**a**) Channel height 1.8 mm; (**b**) Channel height 2.9 mm.

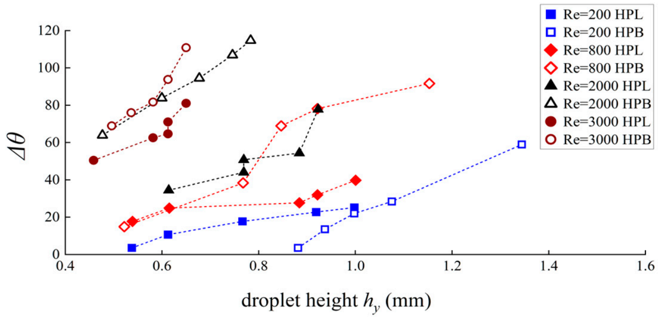

(**a**)

Figure 15: *Cont.*

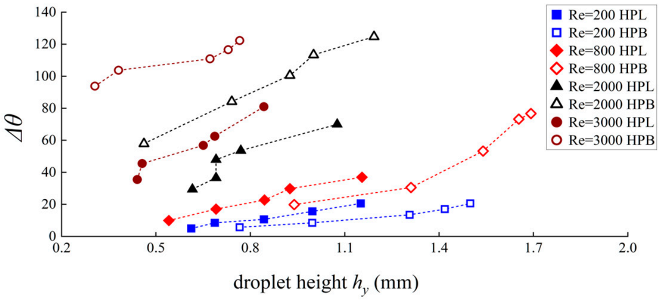

(**b**)

Figure 15: Relationship between the difference in contact angle $\Delta\theta$ (°) and droplet height h_y (mm) under the action of incoming flow for a channel with a width of 3.2 mm: (**a**) Channel height 2 mm; (**b**) Channel height 3.2 mm.

Figs. 16–18 present the relationship between difference in contact angle $\Delta\theta$ and droplet infiltration diameter d_c under different Reynolds numbers for two types of stainless-steel surface wettability, with different channel widths and heights. It can be seen that $\Delta\theta$ on both surfaces increased as d_c increased. In general, the higher the Re, the more obvious the increase in $\Delta\theta$ with increasing d_c. This phenomenon can be explained as follows: as Re or droplet height (or both) increase, the force of incoming air on the droplet will also increase. To maintain the force balance of the droplet, the hysteresis force correspondingly increases. In addition to the increase in $\Delta\theta$, an increase in d_c is also a way for the droplet to maintain force balance, because as d_c increases, the droplet surface-tension F_{ST} also increases. At the same time, as d_c increases, the contact area between the droplet and the stainless-steel substrate also increases, which results in greater friction between the droplet and the substrate. These factors help maintain the equilibrium state of the droplet. From the perspective of droplet detachment, an increase in d_c can be regarded as an obstacle to smooth droplet removal. In addition, the figures show that the d_c value on the hydrophobic surface is generally smaller than that on the hydrophilic surface. This is because the hydrophobic surface generally has a larger contact angle, which leads to a smaller infiltration diameter of the droplet on the hydrophobic surface. Due to the large contact angle, the droplet is more likely to remain nearly spherical, and thus the infiltration diameter is relatively small. The hydrophobic surface promotes droplet detachment by reducing the wetting diameter dc, which is consistent with the findings of Yu et al. [49] in T-shaped channels.

By contrast, on the hydrophilic surface, the smaller contact angle allows the droplet to spread more easily, resulting in a relatively large infiltration diameter. Therefore, on hydrophobic surfaces, where the infiltration diameter is smaller and the adhesive force is weaker, droplets can maintain a more compact shape. After reaching the critical deformation point, droplets are more likely to break the balance of forces, exhibiting a stronger tendency to separate, sliding along the direction of the airflow and detaching. On hydrophilic surfaces, however, droplets are elongated along the direction of the airflow, spreading out as they move forward, and may break apart.

It should also be noted that, for the hydrophilic surface, when the flow channel is 1.2 mm, except high Reynolds numbers, such as Re = 3000 or 2400, where the droplet is subjected to a stronger incoming airflow and can more readily leave its original position, the increase $\Delta\theta$ with increasing droplet infiltration diameter d_c is relatively small for a given Reynolds number. The main reason for this can be explained as follows: because the flow channel is narrow and it is difficult to ensure that the micro-hole is located exactly at the channel center during micro-hole processing, the growing droplet is more likely to come into contact with the side wall of the flow channel. As a result, it becomes difficult for the droplet to reach a free detachment state without interference from the side wall. Therefore, the entire process of droplet growth and adhesion breaking involves relatively small values of d_c and $\Delta\theta$.

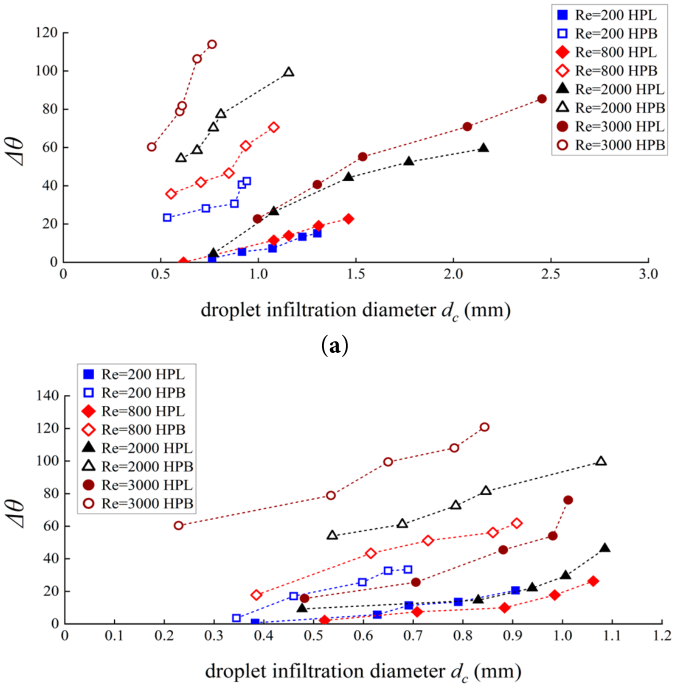

Figure 16: Relationship between the difference in contact angle $\Delta\theta$ ($^\circ$) and droplet infiltration diameter d_c (mm) under the action of incoming flow for a channel with a width of 1.2 mm: (**a**) Channel height 0.9 mm; (**b**) Channel height 2 mm.

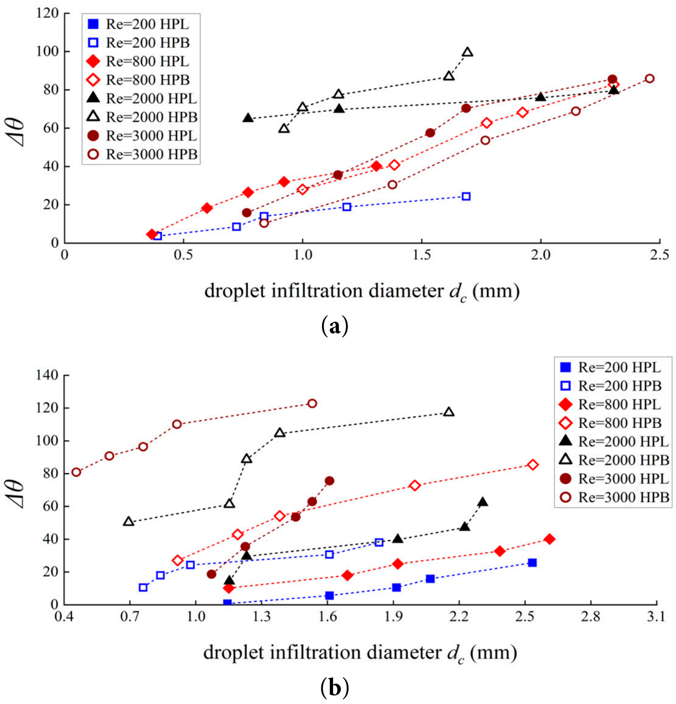

Figure 17: Relationship between the difference in contact angle $\Delta\theta$ ($^\circ$) and droplet infiltration diameter d_c (mm) under the action of incoming flow for a channel with a width of 2.2 mm: (**a**) Channel height 1.8 mm; (**b**) Channel height 2.9 mm.

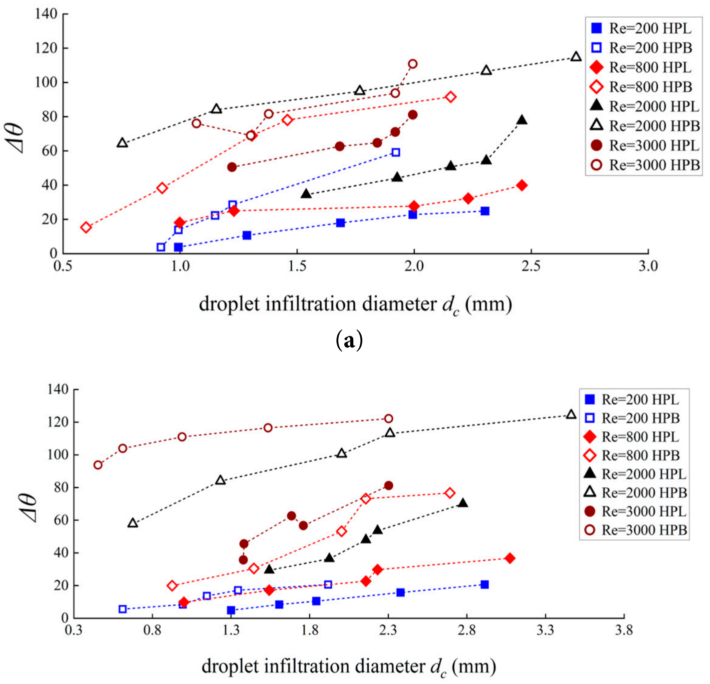

(**a**)

(**b**)

Figure 18: Relationship between the difference in contact angle $\Delta\theta$ (°) and droplet infiltration diameter d_c (mm) under the action of incoming flow for a channel with a width of 3.2 mm: (**a**) Channel height 2 mm; (**b**) Channel height 3.2 mm.

Furthermore, comparative experiments conducted at different seepage rates, where the seepage rate in this study was 10 μL/min and the comparison cases were 30 μL/min and 50 μL/min, indicate that seepage rate does not have a significant effect on the droplet detachment state. However, the time required for the droplet to leave the bottom plate or adhere to the side wall is significantly reduced. This is mainly because droplet deformation under the action of incoming airflow is a transient process, and changes in seepage rate have only a limited influence on the internal stress state of the droplet.

5 Conclusions

Based on the theoretical analysis, the experimental results of single-droplet visualisation were processed and analyzed in this study, with a focus on droplet behavior under two different surface wettabilities. Based on the analysis of the experimental results, the following main conclusions can be drawn:

(1) Correlation among Re, h_y and θ_A. At a constant Re, θ_A on the hydrophobic surface was obviously larger than that on the hydrophilic surface. In addition, θ_A on both surfaces increased with increasing droplet height, and this effect became more pronounced as Re increased. Experimental results further showed that the maximum θ_A on the hydrophobic surface did not always occur at the maximum Re, but was often observed at Re = 2000 or 2400.

(2) Correlation among Re, h_y and θ_R. For a given Re and flow-channel size, droplet height increased while the receding contact angle decreased. When the Re is large ($2000 < \text{Re} < 3000$), the θ_R of the droplet was generally small and the θ_R of the hydrophilic surface was larger, while when Re was small ($200 < \text{Re} < 800$), the effect of droplet height on θ_R was not obvious, θ_R remained relatively larger, and θ_R on the hydrophobic surface was larger than that on the hydrophilic surface.

(3) Correlation among Re, h_y and $\Delta\theta$. The $\Delta\theta$ values on both surfaces increased significantly with increasing Re. At the same time, when the Re was kept constant, $\Delta\theta$ increased with increasing droplet height. The higher the Re, the greater the increase in $\Delta\theta$. At high Re, $\Delta\theta$ on the hydrophobic surface was significantly larger than that on the hydrophilic surface. The magnitude of $\Delta\theta$ was also related to flow-channel size. When both Re and droplet height were fixed, $\Delta\theta$ decreases to some extent as flow-channel height increased.

(4) For the two types of stainless-steel surfaces considered in this study, when the other flow parameters were the same, both θ_A and $\Delta\theta$ on the hydrophobically treated surface were generally larger than those on the untreated stainless-steel surface. By contrast, θ_R on the hydrophobic surface was larger only at low Re. In addition, the droplet infiltration diameter, d_c on the hydrophobic surface was generally smaller than that on the hydrophilic surface, indicating that the droplet on the hydrophobic surface could detach more easily under incoming flow. These results provide theoretical support for the use of hydrophobic surface to improve drainage efficiency.

6 Limitations

(1) The primary objective of this study was to investigate the effects of two distinct solid surface characteristics (hydrophilicity and hydrophobicity) on droplets. We examined the influence of various parameters on the behavior of droplets and summarized the interactions among these physical parameters. However, relying solely on a single hydrophobic treatment has limitations in reflecting the diversity of hydrophobic technologies. Future research should further compare various hydrophobic structures and explore the synergistic effects of different hydrophobic surfaces on contact angle hysteresis and the dynamic deformation rate of droplets.

(2) We ensured surface stability during the experiments through the experimental setup, experimental protocol design, and material selection; however, further research on surface aging under long-term environmental conditions is a necessary step for future engineering applications.

(3) The theoretical model presented in this paper provides a physical benchmark, while the experimental section focuses on phenomenal characterization; the two are logically complementary and exhibit logical consistency in revealing droplet dynamic behavior. However, we acknowledge that, in the absence of support from numerical simulations such as CFD, the degree of coupling between the model and experiments indeed needs to be improved.

Acknowledgement: Not applicable.

Funding Statement: This research was funded by Henan Province Foreign Intelligence Import Program (GZS2020003) and Henan Province Science and Technology Research Project (222102320068).

Author Contributions: The authors confirm contribution to the paper as follows: conceptualization, Jian Li; methodology, Jian Li; validation, Jian Li, Kexiang Wen, Jian Wei; investigation, Kexiang Wen, Jian Wei, Dengke Wen, Ruihao Sun; writing—original draft preparation, Jian Li; writing—review and editing, Jian Li, Kexiang Wen, Jian Wei. All authors reviewed and approved the final version of the manuscript.

Availability of Data and Materials: Data available on request from the authors. The data that support the findings of this study are available from the corresponding author, Jian Li, upon reasonable request.

Ethics Approval: Not applicable.

Conflicts of Interest: The authors declare no conflicts of interest.

Nomenclature

Acronyms and abbreviations widely used in text	
HPL	hydrophilic surface
HPB	hydrophobic surface
Re	Reynolds number
Nomenclature	
C_D	the drag coefficient of the droplet
θ_A	the advancing contact angle (°)
θ_R	the receding contact angle (°)
$\Delta\theta$	the difference in contact angle (°)
θ_Y	Young contact angle (°)
σ_{SL}	interfacial tension at the solid-liquid interface (N/m)
σ_{SG}	interfacial tension at the solid-gas interface (N/m)
σ_l	interfacial tension at a free interface (N/m)
F_D	Wind force (N)
F_{ST}	the combined force of σ_{SG}, σ_{SL}, σ_{LG} and f(N)
∇	Gradient operator
A	the windward area of the droplet (mm^2)
$\overline{u}$	average velocity of incoming flow (m/s)
$\overline{u}_l$	average velocity of droplets on the windward side (m/s)
$\overline{u}_{droplet}$	the average gas velocity on the droplet surface (m/s)
h_y	droplet height (mm)
d_c	droplet infiltration diameter (mm)
Greek Symbols	
θ	contact angle (°), $\theta_R < \theta < \theta_A$
f	hysteresis tension (N/m)
σ	interfacial tension (N/m)
ν	kinematic viscosity (m^2/s)
μ	dynamic viscosity (N·s/m^2)
ρ	density (kg/m^3)

References

1. Chen ZH, Utaka Y, Xu JY, Wang YQ. Freezing characteristics of supercooled water in gas diffusion layer of proton exchange membrane fuel cells. Int J Hydrogen Energy. 2023;48(65):25527–37. [CrossRef].
2. Cho SC, Wang Y. Two-phase flow dynamics in a microchannel with heterogeneous surfaces. Int J Heat Mass Transf. 2014;71:349–60. [CrossRef].
3. Lv X, Chen L, He YL, Tao WQ. Investigation of droplet dynamic in PEMFC gas diffusion layer and gas channel with Micro-CT and lattice Boltzmann method. Fuel. 2025;381:133677. [CrossRef].
4. Mondal N, Biswas D, Bakli C. Improving water removal efficiency in a PEM fuel cell: Microstructured surfaces for controlling instability-driven pinching. APL Energy. 2023;1(3):036105. [CrossRef].
5. Zhu X, Sui PC, Djilali N. Three-dimensional numerical simulations of water droplet dynamics in a PEMFC gas channel. J Power Sources. 2008;181(1):101–15. [CrossRef].
6. Cai YH, Hu J, Ma HP, Yi BL, Zhang HM. Effects of hydrophilic/hydrophobic properties on the water behavior in the micro-channels of a proton exchange membrane fuel cell. J Power Sources. 2006;161(2):843–8. [CrossRef].
7. Molaeimanesh G, Akbari MH. Water droplet dynamic behavior during removal from a proton exchange membrane fuel cell gas diffusion layer by Lattice-Boltzmann method. Korean J Chem Eng. 2014;31(4):598–610. [CrossRef].
8. Chen L, He YL, Tao WQ. Effects of surface microstructures of gas diffusion layer on water droplet dynamic behaviors in a micro gas channel of proton exchange membrane fuel cells. Int J Heat Mass Transf. 2013;60:252–62. [CrossRef].
9. Mondal N, Biswas D, Mukherjee R, Bakli C. Touchdown dynamics of a liquid droplet on a patterned substrate: A generalized lumped parameter-based model. Phys Fluids. 2023;35(8):082117. [CrossRef].

10. Bagherighajari F, Moradi Bilondi A, Abdollahzadehsangroudi M, Hamrang A, Páscoa JC. A parametric numerical study on the performance of polymer electrolyte membrane fuel cell with intermediate-blocked interdigitated flow field designs. Fuel Cells. 2023;23(4):304–22. [CrossRef].
11. Moradi Bilondi A, Bagherighajari F, Abdollahzadehsangroudi M, Kermani MJ, Páscoa JC. The role of porous carbon inserts on the performance of polymer electrolyte membrane fuel cells: A parametric numerical study. Energy Technol. 2022;10(12):2200966. [CrossRef].
12. Hamrang A, Abdollahzadeh M, Bilondi AM, Bagherighajari F, Rahgoshay SM, Pascoa JC. Comparison of PEMFC performance with parallel serpentine and parallel serpentine-baffled flow fields under various operating and geometrical conditions; a parametric study. Int J Hydrogen Energy. 2023;48(20):7442–59. [CrossRef].
13. Huh D, Kuo CH, Grotberg JB, Takayama S. Gas-liquid two-phase flow patterns in rectangular polymeric microchannels: effect of surface wetting properties. New J Phys. 2009;11:75034. [CrossRef].
14. Misiiuk K, Lowrey S, Blaikie R, Juras J, Sommers A. Development of a coating-less aluminum superhydrophobic gradient for spontaneous water droplet motion using one-step laser-ablation. Langmuir. 2022;38(6):1954–65. [CrossRef].
15. Gong L, Yang W, Sun Y, Zhou C, Wu F, Zeng H. Fabricating tunable superhydrophobic surfaces enabled by surface-initiated emulsion polymerization in water. Adv Funct Mater. 2023;33(18):2214947. [CrossRef].
16. Kim SH, Kang HS, Sohn EH, Chang BJ, Park IJ, Lee SG. A strategy for preparing controllable, superhydrophobic, strongly sticky surfaces using SiO_2@PVDF raspberry core-shell particles. RSC Adv. 2021;11(38):23631–6. [CrossRef].
17. Nthunya LN, Gutierrez L, Khumalo N, Derese S, Mamba BB, Verliefde AR, et al. Superhydrophobic PVDF nanofibre membranes coated with an organic fouling resistant hydrophilic active layer for direct-contact membrane distillation. Colloids Surf A Physicochem Eng Asp. 2019;575:363–72. [CrossRef].
18. Tan X, Huang Z, Jiang L, Xiao T, Wang Y, Yang X, et al. A simple fabrication of superhydrophobic PVDF/SiO_2 coatings and their anti-icing properties. J Mater Res. 2021;36(3):637–45. [CrossRef].
19. Kalhor A, Rasuli R. SiO_2-TiO_2@polyvinylidene fluoride nanocomposite: The icephobicity and wettability. Bull Mater Sci. 2022;45(2):91. [CrossRef].
20. Taher MA, Rajput VK, Krishnan PKN, Naraharisetty SR. The validity of triple contact line theory from hydrophilic to super-hydrophobic surfaces. J Phys D Appl Phys. 2022;55(5):055305. [CrossRef].
21. Peng X, Tian D, Li J, Li W, Jiang R, Chen C. Construction of robust electrothermal superhydrophobic surface via femtosecond laser for anti-icing and deicing. Molecules. 2025;30(8):1741. [CrossRef].
22. Cui J, Zhang Y, Wang Y, Yang G. Experimental study on the preparation of superhydrophobic coatings and droplet impact characteristics by laser texturing/hydrothermal deposition coupling. Results Eng. 2025;28:107253. [CrossRef].
23. Owejan JP, Trabold TA, Jacobson DL, Arif M, Kandlikar SG. Effects of flow field and diffusion layer properties on water accumulation in a PEM fuel cell. In: Proceedings of the ASME 2007 5th International Conference on Nanochannels, Microchannels, and Minichannels; 2007 Jun 18–20; Puebla, Mexico. p. 311–20. [CrossRef].
24. Chun JH, Park KT, Jo DH, Lee JY, Kim SG, Park SH, et al. Development of a novel hydrophobic/hydrophilic double micro porous layer for use in a cathode gas diffusion layer in PEMFC. Int J Hydrogen Energy. 2011;36(14):8422–8. [CrossRef].
25. Wang CK, Chan KW, Shen MY, Kuan YD. Titanium felt coated with PTFE as a gas diffuser for proton exchange membrane fuel cell. Int J Hydrogen Energy. 2025;148:149677. [CrossRef].
26. Lee H, Pratama JN, Lee S, Min HJ, Shin D, Bae B. Solvent-optimized PTFE surface treatment for durable hydrocarbon electrolyte membranes in PEMFC. Electrochem Soc Meet Abstr. 2025;248(48):3545. [CrossRef].
27. San FGB, Isik-Gulsac I. Effect of surface wettability of polymer composite bipolar plates on polymer electrolyte membrane fuel cell performances. Int J Hydrogen Energy. 2013;38(10):4089–98. [CrossRef].
28. Yu Q, Chen X, Li X, Zhang D. Optimized design of droplet micro-mixer with sinusoidal structure based on Pareto genetic algorithm. Int Commun Heat Mass Transf. 2022;135:106124. [CrossRef].
29. Chen JH, Lou Q. An Investigation on the immiscible displacement in porous media with contact angle hysteresis. Appl Math Mech. 2021;42(09):900–14. [CrossRef].
30. Xiu Y, Zhu L, Hess DW, Wong CP. Relationship between work of adhesion and contact angle hysteresis on super-hydrophobic surfaces. J Phys Chem C. 2008;112(30):11403–7. [CrossRef].

31. Song YJ. Droplet spreading characteristics on ultra-slippery solid hydrophilic surfaces [dissertation]. Dalian, China: Dalian University of Technology; 2022.
32. Wang J, Wu Y, Cao Y, Li G, Liao Y. Influence of surface roughness on contact angle hysteresis and spreading work. Colloid Polym Sci. 2020;298(08):1107–12. [CrossRef].
33. Chen KS, Hickner MA, Noble DR. Simplified models for predicting the onset of liquid water droplet instability at the gas diffusion layer/gas flow channel interface. Int J Energy Res. 2005;29(12):1113–32. [CrossRef].
34. Tian L, Qiu L. Modeling the wettability of microstructured hydrophobic surface using Multiple-relaxation-time Lattice Boltzmann Method. J Bionic Eng. 2022;19(5):1460–71. [CrossRef].
35. Du WQ, Wu YZ. Comparison of hypsometry and goniometry in contact angle measurement. J Text Res. 2007;28(07):29–37. [CrossRef].
36. Zhang SW, Lian YY. Water repplellence and contact angle measurement. Mod Metrol Test. 1994;3:36–41. [CrossRef].
37. Civan F. Model for interpretation and correlation of contact angle measurements. J Colloid Interface Sci. 1997;192(2):500–2. [CrossRef].
38. De Gennes PG. Wetting: Statics and dynamics. Rev Mod Phys. 1985;57(3):827. [CrossRef].
39. Kwok DY, Budziak CJ, Neumann AW. Measurements of static and low rate dynamic contact angles by means of an automated capillary rise technique. J Colloid Interface Sci. 1995;173(1):143–50. [CrossRef].
40. Sun CG, Zhang HS. Tribological properties of octadecyltrichlorosilane self-assembled monolayers prepared on aluminium metal film. J Dalian Marit Uni. 2008;34(3):34–42.
41. Makkonen L. Young's equation revisited. J Phys-Condens Matter. 2016;28(13):135001. [CrossRef].
42. Adam NK. Use of the term 'Young's Equation'for contact angles. Nature. 1957;180(4590):809–10. [CrossRef].
43. Bormashenko E, Bormashenko Y, Whyman G, Pogreb R, Musin A, Jager R, et al. Contact angle hysteresis on polymer substrates established with various experimental techniques, its interpretation, and quantitative characterization. Langmuir. 2008;24(8):4020–5. [CrossRef].
44. Kulinich SA, Farzaneh M. Effect of contact angle hysteresis on water droplet evaporation from super-hydrophobic surfaces. Appl Surf Sci. 2009;255(7):4056–60. [CrossRef].
45. Min JC, Peng XF, Wang XD. Departure diameter of a drop on a vertical plate. J Basic Sci Eng. 2002;10(1):57–62. [CrossRef].
46. Wang X, Peng X, Zhang X. Investigation on critical airflow velocity about departure of droplet from horizontal wall. J Basic Sci Eng. 2006;14(3):403–10. [CrossRef].
47. Korte C, Jacobi AM. Condensate retention effects on the performance of plain-fin-and-tube heat exchangers: Retention data and modeling. ASME J Heat Transf. 2001;123(5):926–36. [CrossRef].
48. Al-Hayes RAM, Winterton RHS. Bubble diameter on detachment in flowing liquids. Int J Heat Mass Transf. 1981;24(2):223–30. [CrossRef].
49. Yu Q, Chen X. Insights into the breaking and dynamic mixing of microemulsion (W/O) in the T-junction microchannel. Chaos Solitons Fractals. 2022;155:111774. [CrossRef].